CrossMark

Constraining Planetary Gas Accretion Rate from Hα Line Width and Intensity: Case of PDS 70 b and c

Yuhiko Aoyama[1,2,3] and Masahiro Ikoma[1,4]

[1] Department of Earth and Planetary Science, Graduate School of Science, The University of Tokyo, 7-3-1 Hongo, Bunkyo-ku, Tokyo 113-0033, Japan; yaoyama@tsinghua.edu.cn
[2] Institute for Advanced Study, Tsinghua University, Beijing 100084, People's Republic of China
[3] Department of Astronomy, Tsinghua University, Beijing 100084, People's Republic of China
[4] Research Center for the Early Universe (RESCEU), Graduate School of Science, The University of Tokyo, 7-3-1 Hongo, Bunkyo-ku, Tokyo 113-0033, Japan

Abstract

Recent observations of protoplanets embedded in circumstellar disks have shed light on the planet formation process. In particular, detection of hydrogen Balmer-line (Hα) emission gives direct constraints on late-stage accretion onto gas giants. Very recently Haffert et al. measured the spectral line widths, in addition to intensities, of Hα emission from the two protoplanets orbiting PDS 70. Here, we study these protoplanets by applying radiation-hydrodynamic models of the shock-heated accretion flow onto protoplanets that Aoyama et al. have recently developed. As a result, we demonstrate that Hα line widths combined with intensities lead to narrowing down the possible ranges of the protoplanetary accretion rate and/or mass significantly. While the current spectral resolution is not high enough to derive a definite conclusion regarding their accretion process, high-resolution spectral imaging of growing protoplanets is highly promising.

1. Introduction

Observation of growing protoplanets is a challenge, but provides crucial constraints on planet formation. Recent detections of Hα emission from young companions embedded in circumstellar gaseous disks sheds light on the late-stage gas accretion onto protoplanets (Close et al. 2014; Sallum et al. 2015; Wagner et al. 2018). Very recently, Haffert et al. (2019) conducted follow-up observation with a high-resolution ($R \sim 2500$) spectral imaging technique and thereby confirmed the previous detection of Hα emission from PDS 70 b. They also detected another source of strong Hα emission, which they identified as a second protoplanet in the PDS 70 system (i.e., PDS 70 c). Not only that, the high-resolution spectral imaging allowed them to obtain Hα line profiles for the two protoplanets.

Such Hα emission is likely to originate from hot portions ($\sim 1 \times 10^4$ K) of infalling accretion flow onto the protoplanet and circumplanetary disk. There is an empirical relation between the mass accretion rate and the full width at 10% of the maximum of the Hα line obtained for T Tauri star (TTS) accretion (e.g., Hartmann et al. 1994; Natta et al. 2004). Haffert et al. (2019) estimated the mass accretion rates at $2 \times 10^{-8 \pm 0.4}$ M_J yr^{-1} and $1 \times 10^{-8 \pm 0.4} M_J$ yr^{-1} for PDS 70 b and c, respectively. This empirical relation is based on the assumption that the accreting gas flowing along the stellar dipole magnetic field lines is hot enough to emit Hα radiation.

Gas accretion for protoplanets, however, may be different from stellar accretion. This is partly because of the fact that the former is much less energetic than the latter due to their much lower mass and, hence, shallower gravitational potential. In the stellar case, high freefall velocity causes a strong shock at the stellar surface, making the accreting gas hot enough to ionize hydrogen completely. This means that hydrogen-line emission is not possible (Hartmann et al. 1994). By contrast, in the planetary case, the moderate shock heating makes a dominant

contribution to Hα emission. To quantify the Hα emission from such shock-heated gas, Aoyama et al. (2018, hereafter AIT18) developed a 1D radiation-hydrodynamic code that simulates nonequilibrium hydrogen-line emission from gas flow behind the accretion shock (see Section 2) and thereby demonstrated that the shock-heated gas generates significant hydrogen-line emission strong enough to be detected.

In this Letter, we report the study of the two accreting protoplanets in the PDS 70 system, applying the models of AIT18. In particular, we demonstrate that the spectral line width along with its intensity (or the Hα luminosity) as observational constraints help us to narrow down the possible ranges of mass accretion rate onto the protoplanets.

2. Model Description

2.1. Gas Accretion Feature

The geometry and flow pattern for protoplanetary accretion remain poorly understood. Some of the accreting gas falls almost freely onto the protoplanet directly, while some settles down onto the circumplanetary disk and migrates toward the central protoplanet. Even in the latter case, the accreting gas eventually falls freely from the inner edge of the circumplanetary disk onto the protoplanet, provided there is a wide gap between the protoplanet and circumplanetary disk (or an inner cavity; Koenigl 1991). This is similar to the situation often considered and thus studied well in the case of the accretion of TTSs (e.g., see the review of Hartmann et al. 2016).

Both types of accretion flow would require a strong dipole magnetic field for the protoplanet. Its existence is predicted according to the scaling law between the luminosity and magnetic field strength of astronomical objects (Christensen et al. 2009). Also, the predicted magnetic field of an accreting gas giant is strong enough to affect the accretion flow pattern (Batygin 2018).

2.2. Modeling of Hα Emission

A common feature in both cases is that the gas flow collides with the protoplanet's surface at the a freefall velocity. Since the freefall velocity is higher than the local sound one, the gas flow passes through shockwaves there. Shock compression heats the gas to a temperature on the order of 10^4 K, which is high enough to dissociate hydrogen molecules and ionize some of the hydrogen atoms, producing free electrons. The electrons collide with and excite the hydrogen atoms. De-excitation of the excited hydrogen results in line emission and cooling.

With the numerical code developed by Aoyama et al. (2018), we simulate the radiation hydrodynamics of the 1D gas flow behind the shock front, including calculations of chemical reactions, excitation/de-excitation of hydrogen atoms, and radiative transfer. The collisional and radiative transitions of energy levels in hydrogen atoms are calculated in a time-dependent way with the transition rate coefficients from Vriens & Smeets (1980). As demonstrated in Aoyama et al. (2018), since the shock-heated gas cools immediately and the Hα emission occurs only in a thin layer below the shock front, the plane-parallel (or 1D) approximation is valid. We assume an ideal gas mixture with the solar elemental abundances from Allen (1976). The input parameters are the pre-shock velocity v_0 and the number density of hydrogen nuclei n_0. The details of the AIT18 model are given in Section 2 of Aoyama et al. (2018).

3. Theoretical Emission Property

3.1. Spectral Line Width

First, we demonstrate that our 1D radiation-hydrodynamic models yield Hα line profiles that are consistent with the ones for PDS 70 b and c observed with the Multi Unit Spectroscopic Explorer (MUSE)/Very Large Telescope (VLT) by Haffert et al. (2019). Figure 1 compares the observed spectral emission profiles with simulated ones. The assumed values of the pre-shock velocity v_0 and the number density of hydrogen nuclei n_0 in our shock model are $v_0 = 150$ km s^{-1} and $n_0 = 1 \times 10^{20}$ m^{-3} for PDS 70 b (upper panel) and $v_0 = 130$ km s^{-1} and $n_0 = 1 \times 10^{19}$ m^{-3} for PDS 70 c (lower panel). (Note that these sets of v_0 and n_0 yield the full widths at 10% and 50% of the maximum of the protoplanet's Hα emission lines that are consistent with the observed values for each planet; see Section 4.1 for the details.) In the upper and lower panels, the red lines indicate the observed signal-to-noise ratio. As for the model profiles, the orange line indicates the raw line energy flux per unit wavelength, while the blue one represents the energy flux smoothed with a filter of $R = 2500$. It does not matter that the quantities on the vertical axis of each panel differ between the synthesized and observed profiles, since the focus is on the spectral profile rather than intensity here. Also, though the wavelength is also arbitrarily shifted, it does not affect the following descriptions.

For more quantitative comparison, rather than the shape of spectral profiles, we also focus on the spectral line width. Haffert et al. (2019) estimated the full widths at 10% and 50% of the maximum of the protoplanet's Hα emission line (simply the Hα 10% and 50% full widths, respectively, hereafter), values listed in Table 1.

Figure 2 shows the calculated Hα 10% full width (left panel) and 50% full width (right panel) as a function of the pre-shock velocity v_0 and number density n_0. In both panels, the Hα full
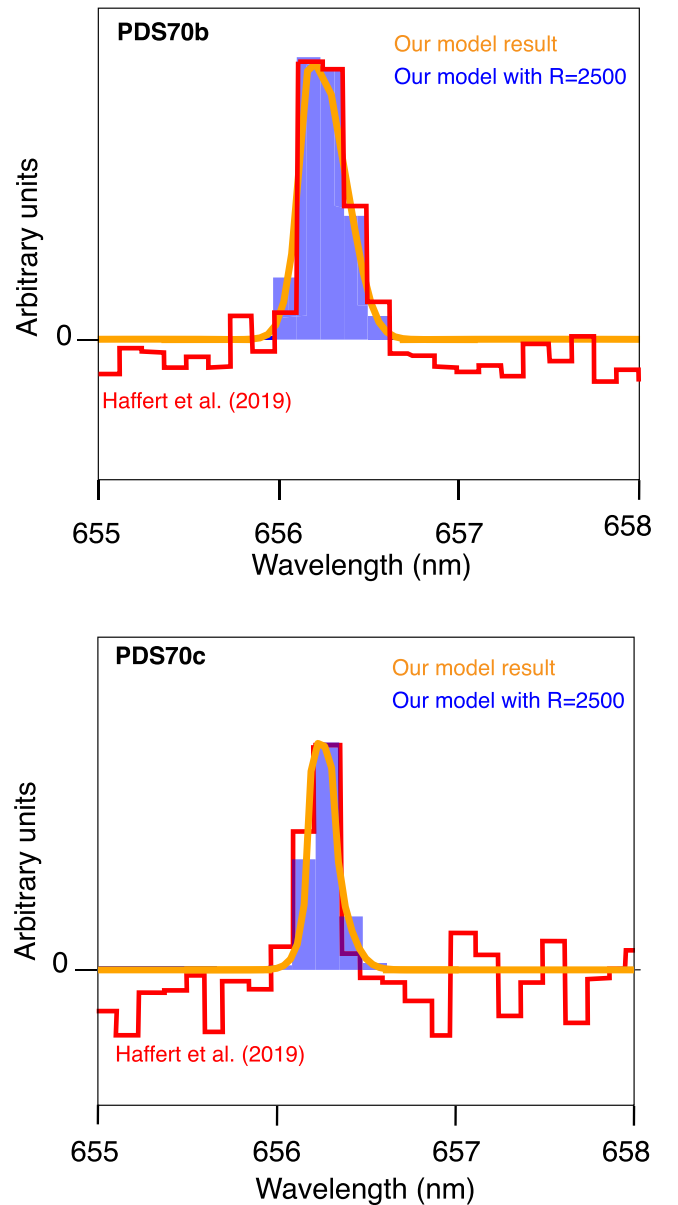

Figure 1. Simulated and observed spectral emission profiles around the Hα line for PDS 70 b (upper panel) and c (lower panel). The observed profiles, which were obtained with MUSE/VLT by Haffert et al. (2019), are indicated by red lines. As for the simulated profiles, the raw data are shown with orange lines, while the data smoothed with a filter of $R = 2500$ are shown with blue bars. Note that the quantities of the vertical axis differ between the observed and calculated data; the observed data are the signal-to-noise ratio, whereas the raw and smoothed calculation data are the energy flux per unit wavelength and just the energy flux, respectively. Also, the calculated profiles have been artificially shifted by -2.5 Å and -2.2 Å for PDS 70 b and c, respectively, so as to coincide with the observed ones.

width increases with pre-shock velocity. This is because a flow with higher velocity passes through a stronger shock and then becomes hotter, enhancing Doppler broadening, which is responsible for the width of the Hα line profile.

Second, it turns out that an increase in the number density results in increasing the Hα full width. This is not due to pressure broadening, which is negligibly small relative to Doppler and natural broadening, but due to the effect of absorption. The Hα radiation, which comes out deep below the shock front, propagates upward through the shock-heated gas toward the shock front. During that propagation, some of the

Table 1
Properties of PDS 70 b and c

	PDS 70 b	PDS 70 c
Hα Observation		
10% full width [km s^{-1}]	224 ± 24 (1)	186 ± 35 (1)
50% full width [km s^{-1}]	123 ± 13 (1)	102 ± 19 (1)
Luminosity [$10^{-7}L_\odot$]	1.6 ± 0.14 (1)	0.76 ± 0.13 (1)
	14 ± 6 (2)	non-detection (2)
Estimated Properties in This Study (3)		
M_P [M_J]	12	10
$\dot{M}$ [$10^{-8}M_J$ yr^{-1}]	4	1
f_f [10^{-3}]	0.50	0.33
Estimated Properties in Previous Studies		
M_P [M_J]	2–17	4–12 (4)
$\dot{M}$ [$10^{-8}M_J$ yr^{-1}]	2 (5), (6)	1 (5), (6)

Note. (1) Haffert et al. (2019), (2) Wagner et al. (2018), (3) Section 4.1, (4) Müller et al. (2018), (5) Haffert et al. (2019), (6) Natta et al. (2004).

Hα radiation is absorbed (Aoyama et al. 2018). The higher the gas density, the stronger the absorption of Hα radiation near the line center. Such a decrease in the line-peak intensity results in an increase in the Hα full width because the latter is measured from the former.

In Figure 2, the observational results from Haffert et al. (2019) are indicated by the black line for PDS 70 b and by the blue line for PDS 70 c with 1σ errors indicated by the same-color shades. From this figure, we obtain possible ranges of v_0 and n_0 for the accretion flow toward the two protoplanets (see Section 4.1 for further discussion).

3.2. Hα Luminosity

The values of the observed Hα luminosity for the two protoplanets reported by Wagner et al. (2018) and Haffert et al. (2019) are listed in Table 1. In our model, we assume that a strong shock occurs at the surface of the protoplanet so that the Hα luminosity is given by

$$L_{H\alpha} = 4\pi R_P^2 f_f F_{H\alpha} 10^{-A'_{H\alpha}}, \qquad (1)$$

where R_P is the planetary radius, f_f is the fractional area of planetary surface where the accretion flow eventually emits Hα radiation, which is termed the filling factor, and $F_{H\alpha}$ is the Hα energy flux per unit area. The factor $10^{-A'_{H\alpha}}$ represents extinction of the Hα radiation on the way from the protoplanet's emission surface to the observer (in addition to interstellar absorption). The extinction is caused by the circumstellar disk, disk wind above the disk, accretion flow toward the protoplanet, and so on. The exact values of f_f and $A'_{H\alpha}$ are poorly known.

Figure 3 shows the calculated value of $L_{H\alpha}$ as a function of the protoplanet mass M_P and the planetary mass accretion rate $\dot{M}$; the latter is given by

$$\dot{M} = 4\pi R_P^2 f_f \ \mu' n_0 v_0, \qquad (2)$$

where μ' is the mean weight per hydrogen nucleus. Also, since the pre-shock velocity is assumed to be the freefall one, the planetary mass is related to v_0 as

$$M_P = \frac{R_P v_0^2}{2G}, \qquad (3)$$

where G is the gravitational constant. Here we have assumed $R_P = 2 \ R_J$ and $f_f = 1$. In this figure, the Hα luminosity is found to be almost proportional to protoplanet mass and mass accretion rate (i.e., $L_{H\alpha} \propto \dot{M}M_P$) for the following reason: from Equations (1)–(3),

$$L_{H\alpha} = \dot{M} \frac{2GM_P}{R_P} \frac{F_{H\alpha}(v_0, n_0)}{\mu' n_0 v_0^3} 10^{-A'_{H\alpha}}. \qquad (4)$$

Aoyama et al. (2018) found $F_{H\alpha}$ is roughly proportional to $n_0 v_0^3$. Note that although absent in Equation (4), the filling factor f_f affects $L_{H\alpha}$ somewhat, because $F_{H\alpha}/(n_0 v_0^3)$ is roughly constant but varies with n_0 due to optical-depth effects, and n_0 depends on f_f as shown in Equation (2). However, f_f is still less important than the other parameters for $L_{H\alpha}$.

In Figure 3, like in Figure 2, we indicate the observational results from Wagner et al. (2018) and Haffert et al. (2019). Infrared observations estimate the masses of PDS 70 b and c at 2–17 M_J (Müller et al. 2018) and 4–12 M_J (Haffert et al. 2019), respectively. According to Figure 3, in those ranges of protoplanet mass, the mass accretion rate for PDS 70 b is $\sim 1 \times 10^{-7}$ M_J yr^{-1} for the data from Wagner et al. (2018) and $\sim 1 \times 10^{-8}$ M_J yr^{-1} for the data from Haffert et al. (2019), while that for PDS 70 c is $\sim 1 \times 10^{-8}$ M_J yr^{-1}. We discuss the difference in estimated mass accretion between the present and previous studies in Section 4.2.

Note that we have assumed that all of the accreting gas falls onto the surface of the protoplanet, as in the above studies (Wagner et al. 2018; Haffert et al. 2019). Since the focus of this study is on the effect of the accretion shock on the Hα emission, detailed treatment of accretion flow toward the protoplanetary system including the circumplanetary disk is beyond the scope of this study. A further detailed investigation is done in our forthcoming paper (Y. Aoyama et al. 2019, in preparation).

4. Discussion

4.1. Gas Accretion Rates for PDS 70 b and c

Combining the three kinds of observational datum, the Hα luminosity, 10% full width, and 50% full width, we narrow the possible ranges of the mass accretion rate and protoplanet mass for the two accreting protoplanets. In Figure 4, we show again the v_0–n_0 relationships for PDS 70 b and c derived from our models with all three observational constraints. Since the theoretical estimate of Hα luminosity depends on two uncertain parameters, namely, f_f and $A'_{H\alpha}$ (see Equation (1)), we show the v_0–n_0 relationships for two different choices of $10^{A'_{H\alpha}} f_f^{-1}$ or $A'_{H\alpha} - \log f_f = 2$ and 3. While correct values of $A'_{H\alpha}$ and f_f are poorly understood for the case of planetary accretion, we note that their ranges are constrained in the context of accreting TTS: theoretical modeling of accretion shocks with $f_f = \sim 10^{-5}$ –10^{-1} reproduces observed UV excesses of TTSs (e.g., Table 12 of Herczeg & Hillenbrand 2008). Also, Wagner et al. (2018) assumed $0 \lesssim A'_{H\alpha} \lesssim 3$ as a likely range of $A'_{H\alpha}$.

The intersection point of the two lines of the maximum likelihood values for 10% and 50% full widths is $(v_0, n_0) = (145$ km s^{-1}, 6×10^{19} m^{-3}) for PDS 70 b and
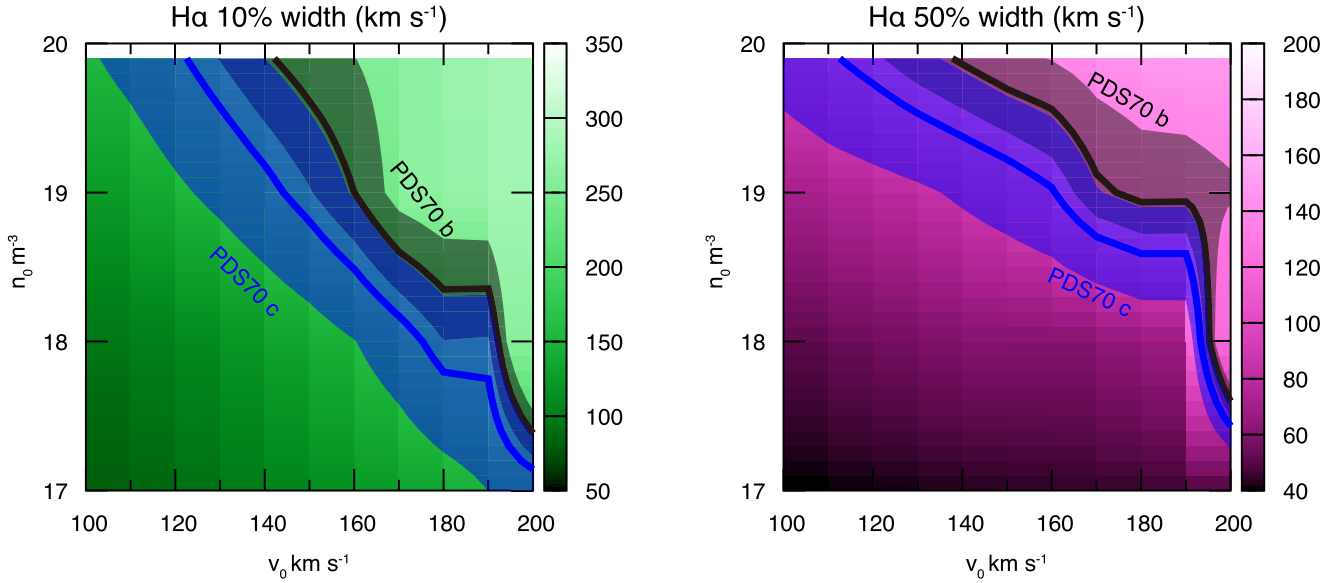
Figure 2. Full width at 10% (left panel) and 50% (right panel) of the maximum of the protoplanet's Hα emission line. Contour plots of the full width are shown as functions of the pre-shock velocity v_0 and number density n_0. In each panel, the maximum likelihood values and 1σ errors of the observed widths from Haffert et al. (2019) are represented by thick lines and shaded areas, respectively; black and blue are for PDS 70 b and c, respectively.
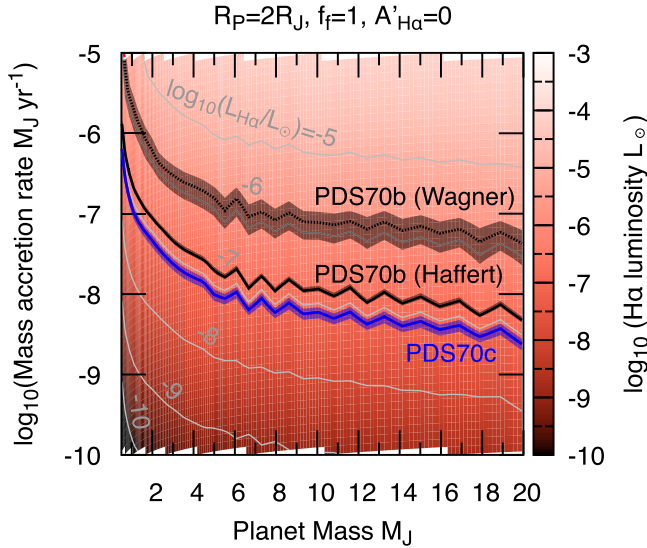

Figure 3. Color contour plot of the protoplanet's Hα luminosity as a function of protoplanet mass and mass accretion rate. As indicated in the figure, the lines and shaded areas represent the observed maximum likelihood values and 1σ errors of Hα luminosity for PDS 70 b, $(1.4 \pm 0.6) \times 10^{-6} L_\odot$ (black dashed line; Wagner et al. 2018) and $(1.6 \pm 0.14) \times 10^{-7} L_\odot$ (black solid line; Haffert et al. 2019), and PDS 70 c, $(7.6 \pm 1.3) \times 10^{-8} L_\odot$ (blue line; Haffert et al. 2019). The gray thin lines are contour lines for Hα luminosities of 10^{-5}–$10^{-10} L_\odot$. Here, we have assumed the protoplanet radius $R_P = 2R_J$, the filling factor $f_f = 1$, and the extinction $A'_{H\alpha} = 0$.

$(130 \ \mathrm{km \ s^{-1}}, 3 \times 10^{19} \ \mathrm{m^{-3}})$ for PDS 70 c. To reproduce the observed Hα luminosity, the value of $10^{A'_{H\alpha}} f_f^{-1}$ comes out to be 2×10^3 and 3×10^3 for PDS 70 b and c, respectively.

To convert (v_0, n_0) to $(M_P, \dot{M})$, we assume $A'_{H\alpha} = 0$ and $R_P = 2R_J$. Then, substituting the values of v_0, n_0, and f_f estimated above into Equations (2) and (3), we obtain $(M_P, \dot{M})$ as $(12M_J, 4 \times 10^{-8} M_J \ \mathrm{yr^{-1}})$ and $(10M_J, 1 \times 10^{-8} M_J \ \mathrm{yr^{-1}})$ for PDS 70 b and c, respectively. The estimated values are listed in Table 1. The assumption of $A'_{H\alpha} = 0$ is a reasonable one, given that the gas falling onto the protoplanet is depleted of dust and thus optically thin in the late stages of planet formation (see

also G. D. Marleau & Y. Aoyama, in preparation). Also, the resultant value of $f_f \sim 10^{-3}$ is similar to that for the case of accretion shocks for low-mass stars (Herczeg & Hillenbrand 2008). However, given the importance of the filling factor, detailed numerical simulations of protoplanetary gas accretion should be done to determine the exact value of f_f.

4.2. Comparison with Previous Models

Wagner et al. (2018) and Haffert et al. (2019) also estimated the mass accretion rate onto PDS 70 b and/or c, based on empirical relationships derived from observations of accreting, low-mass TTSs. Here, we discuss the difference between our model and the previous models, which yield different estimates of the mass accretion rates $\dot{M}$.

To estimate $\dot{M}$ from the observed Hα luminosity $L_{H\alpha}$ for PDS 70 b, Wagner et al. (2018) used the empirical formula derived by Rigliaco et al. (2012), which gives a relationship between $L_{H\alpha}$ and the continuum integrated over all wavelengths L_{acc}. They assumed that the latter (i.e., L_{acc}) was related directly to the mass accretion rate. For $A'_{H\alpha} = 0$, for example, their estimated $\dot{M}$ is $10^{-8.7\pm0.3} M_J \ \mathrm{yr^{-1}}$. This value is smaller by one to two orders of magnitude than our estimate (see the black dotted line in Figure 3). This difference comes from the fact that hydrogen-line emission accounts for a significant fraction of the total emission for the protoplanetary case, in contrast to the case of TTSs (see Section 4.3 for details). Relationships between $L_{H\alpha}$ and L_{acc} and between $L_{H\alpha}$ and $\dot{M}$ applicable to planetary accretion are presented in our forthcoming paper (Y. Aoyama et al. 2019, in preparation).

Haffert et al. (2019) estimated the mass accretion rate to be $2 \times 10^{-8\pm0.4} M_J \ \mathrm{yr^{-1}}$ and $1 \times 10^{-8\pm0.4} M_J \ \mathrm{yr^{-1}}$ for PDS 70 b and c, respectively, from the empirical relationship between the mass accretion rate and the Hα 10% full width derived by Natta et al. (2004). These values are, by chance, similar to our estimates given in Section 4.1. The process of Hα emission, however, definitely differs between their and our models: in contrast to our model, Natta et al. (2004) considered that preshock gas flowing toward TTSs (not shock-heated gas) is hot
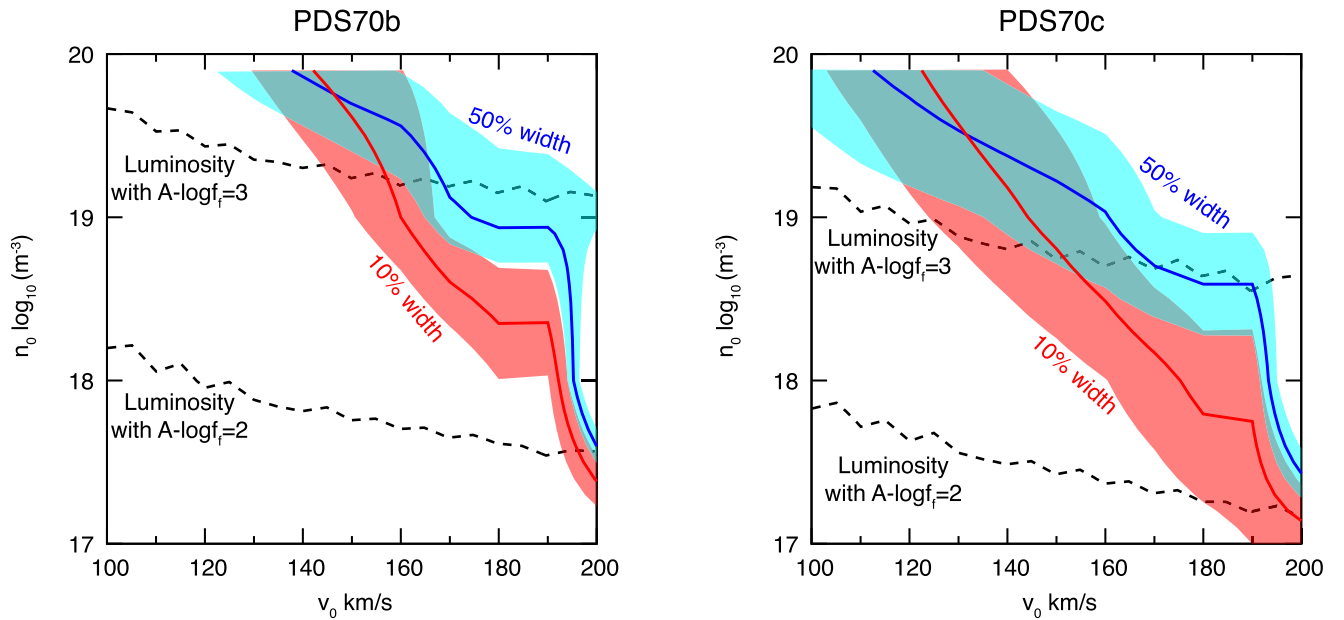
Figure 4. Properties of accretion shock on the protoplanetary surface inferred with three different observational constraints including the Hα luminosity, 10% full width, and 50% full width. The red and blue lines correspond to the maximum likelihood values of the Hα 10% width and 50% width, respectively (see also Figure 2). The black dotted lines represent the observed Hα luminosity for two choices of the uncertain parameter $f_f 10^{-A}$ (see Equation (1)), namely, $A'_{H\alpha} - \log f_f = 2$ and 3.

enough to generate Hα emission. For different choices of f_f and $A'_{H\alpha}$, the estimated value of $\dot{M}$ differs considerably between the models. Combined effects of post-shock emission and the pre-shock emission are of great interest. Therefore, it will be important to conduct a detailed investigation to confirm whether enough heating occurs in the accretion flow for protoplanets.

4.3. Difference between Planetary and Stellar Cases

The key difference between planetary and stellar accretion is in the freefall velocity, shock strength. This determines whether the shock-heated gas becomes hot enough to ionize the hydrogen completely; of course, completely ionized hydrogen never emits Hα radiation. Stellar accretion shocks are strong enough in that sense. Therefore, previous studies of stellar accretion focus on *pre*-shock gas as the source of Hα emission. In contrast, in the case of planetary accretion, the shock-heated gas becomes hot enough to excite but not enough to ionize hydrogen. Thus, the *post*-shock gas is the main source of Hα emission. Pre-shock heating is unlikely for planetary accretion. Therefore, we have applied the post-shock emission model (Aoyama et al. 2018) to the planetary-mass objects PDS 70 b and c in this study.

5. Concluding Remarks

In this study, we have applied our planetary accretion shock model (Aoyama et al. 2018) to the two accreting proto-gas giants, PDS 70 b and c, for which Hα emission fluxes and profiles were very recently observed (Wagner et al. 2018; Haffert et al. 2019). We have demonstrated that the new observational data, namely, spectral profiles, combined with Hα luminosity, help us to narrow down the possible ranges of pre-shock velocity and number density. As a result, better constraints on mass accretion rate and protoplanet mass gives rise to deeper insight into late-stage accretion onto gas giants.

At present, however, the Hα line profiles for the two protoplanets are resolved with only a few wavelength bins. Also, the 10% and 50% full widths, which we have used for constraining the ranges of M_P and $\dot{M}$, are estimated with Gaussian fitting (Haffert et al. 2019). As demonstrated in Section 3.1, not only emission but also absorption of Hα is crucial for constraining the mass accretion rate. Gaussian fitting may not be sufficient to represent the absorbing features. In addition, some theoretical and observational studies of protostellar accretion reported that for some targets, pre-shock gas absorbs a significant amount of the Hα radiation from the post-shock region, giving rise to asymmetric spectral features (e.g., Edwards et al. 1994). On the other hand, no such absorption occurs in the case of protoplanetary Hα emission (Haffert et al. 2019). Higher-resolution spectroscopy is expected to cast light on protoplanetary gas accretion.

Appendix

We demonstrate the effects of the pre-shock velocity v_0 and the hydrogen number density at the shock n_0 on the Hα line profiles in Figure 5. The profile width becomes broader with increasing v_0, because larger v_0 results in hotter gas and thereby causes wider Doppler broadening after the shock. The sensitivity of the width to v_0 is, however, found not to be high. This is because Hα emission mainly comes from deeper regions where the gas cools to $\sim 10^4$ K (see Aoyama et al. 2018) and, therefore, the temperature of the emission region depends little on v_0. Note that a spectral resolution of $R = 2500$ is not sufficient to distinguish such a difference. An increase in
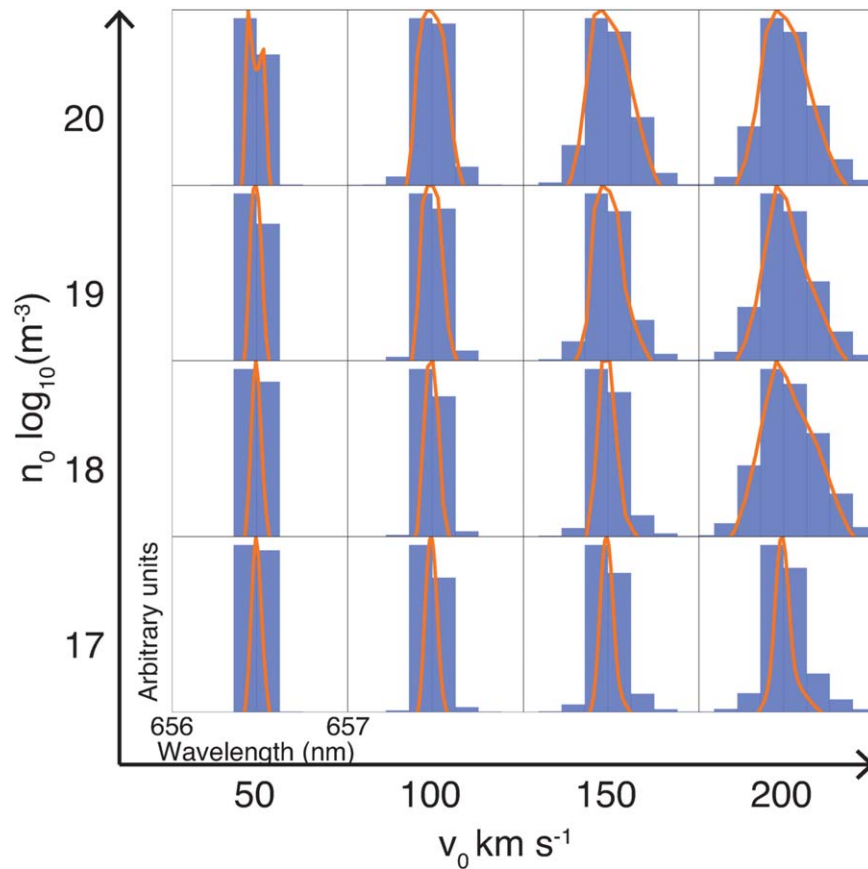
Figure 5. Simulated emission profiles around the Hα line (orange line) for several different choices of the pre-shock velocity, $v_0 = 50$, 100, 150, and 200 km s^{-1} and the hydrogen number density at the shock, $n_0 = 1 \times 10^{17}$, 10^{18}, 10^{19}, and 10^{20} m^{-3}. Each panel is the same as Figure 1, except for the values of v_0 and n_0. The background histogram indicates the simulated emission profiles smoothed over the bins of width 0.13 nm, which corresponds to a resolution of $R = 2500$.

n_0 leads to broadening the profile width, because the contribution of the broad component coming from hot regions just after the shock becomes dominant, as n_0 becomes large (e.g., see the case of $v_0 = 200$ km s^{-1} and $n_0 = 10^{18}$ m^{-3}). This broad component of the profile can be detected with a resolution of $R = 2500$.

ORCID iDs

Yuhiko Aoyama ⓘ https://orcid.org/0000-0003-0568-9225
Masahiro Ikoma ⓘ https://orcid.org/0000-0002-5658-5971

References

Allen, C. W. 1976, Astrophysical Quantities (London: Athlone)

Aoyama, Y., Ikoma, M., & Tanigawa, T. 2018, ApJ, 866, 84
Batygin, K. 2018, AJ, 155, 178
Christensen, U. R., Holzwarth, V., & Reiners, A. 2009, Natur, 457, 167
Close, L. M., Follette, K. B., Males, J. R., et al. 2014, ApJL, 781, L30
Edwards, S., Hartigan, P., Ghandour, L., & Andrulis, C. 1994, AJ, 108, 1056
Haffert, S. Y., Bohn, A. J., de Boer, J., et al. 2019, NatAs, 329, 749
Hartmann, L., Herczeg, G., & Calvet, N. 2016, ARA&A, 54, 135
Hartmann, L., Hewett, R., & Calvet, N. 1994, ApJ, 426, 669
Herczeg, G. J., & Hillenbrand, L. A. 2008, ApJ, 681, 594
Koenigl, A. 1991, ApJL, 370, L39
Müller, A., Keppler, M., Henning, T., et al. 2018, A&A, 617, L2
Natta, A., Testi, L., Muzerolle, J., et al. 2004, A&A, 424, 603
Rigliaco, E., Natta, A., Testi, L., et al. 2012, A&A, 548, A56
Sallum, S., Follette, K. B., Eisner, J. A., et al. 2015, Natur, 527, 342
Vriens, L., & Smeets, A. H. M. 1980, PhRvA, 22, 940
Wagner, K., Follete, K. B., Close, L. M., et al. 2018, ApJL, 863, L8